Arrays of InP-based Avalanche Photodiodes for Photon Counting

Simon Verghese, *Member, IEEE*, Joseph P. Donnelly, *Life Fellow, IEEE*, Erik K. Duerr, K. Alex McIntosh, David C. Chapman, Christopher J. Vineis, Gary M. Smith, *Senior Member, IEEE*, Joseph E. Funk, Katharine Estelle Jensen, Pablo I. Hopman, David C. Shaver, *Senior Member, IEEE*, Brian F. Aull, *Senior Member, IEEE*, Joseph C. Aversa, Jonathan P. Frechette, James B. Glettler, Zong Long Liau, Joseph M. Mahan, Leonard J. Mahoney, *Member, IEEE*, Karen M. Molvar, Frederick J. O'Donnell, Douglas C. Oakley, Edward J. Ouellette, Matthew J. Renzi, and Brian M. Tyrrell, *Member, IEEE*

(Invited Paper)

***Abstract*—Arrays of InP-based avalanche photodiodes (APDs) with InGaAsP absorber regions have been fabricated and characterized in the Geiger mode for photon-counting applications. Measurements of APDs with InGaAsP absorbers optimized for 1.06 μm wavelength show dark count rates (DCRs) $<$20 kHz for room-temperature operation with photon detection efficiency (PDE) up to 50% and a reset or dead time of 1 μs. APDs with InGaAs absorbers optimized for 1.55 μm wavelength and 240 K temperature have DCRs $<$20 kHz, PDE up to 45%, and a reset time of $\sim$6 μs. Arrays for both wavelengths have been fabricated and packaged with GaP microlenses (of 100 and 50 μm pitch) and CMOS readout integrated circuits (ROICs). Comparisons are made between ROICs that operate in the framed-readout mode as well as those that operate in continuous-readout mode.**

***Index Terms*—Avalanche photodiodes (APDs), Geiger-mode APD (GM-APD), InP, photon counting, single photon detection.**

I. Introduction

Avalanche photodiodes (APDs) operating at short-wave infrared wavelengths (SWIR) in the Geiger mode (GM) can detect single photons with $<$0.5 ns timing resolution [1]. Unlike linear-mode APDs, an InP-based GM-APD is temporarily biased several volts beyond its junction-breakdown voltage until it absorbs a signal photon. In less than 1 ns after injecting a photogenerated hole into its InP multiplier, milliamps of multiplied current discharge the cathode by more than a volt for virtually error-free detection of the photon-absorption event by a wide-bandwidth decision circuit. Therefore, GM-APDs have essentially zero readout noise and accommodate low-power, fast-decision circuits. GM-APDs are limited by their 1-bit dynamic range, their dark count rate (DCR) and photon detection efficiency (PDE), and by the minimum reset time or dead time required to avoid afterpulsing. System designers can improve the dynamic range and reduce the effective reset time by using large arrays of GM-APDs bump-bonded to CMOS readout integrated circuits (ROICs). Here, subarrays of pixels are treated as single spatial-resolution elements—often called macropixels. Macropixels use spatial oversampling to build up the effective dynamic range per resolution element.

Two types of active optical systems are driving most of the development of InP GM-APD arrays: imaging laser RADAR (LADAR) and free-space laser communication (LC). Brief descriptions and references follow. Flash LADAR systems use arrays of direct-detection detectors at relatively low duty cycle. Here, bright transmit pulses (1–2 ns) illuminate the target with modest pulse-repetition frequency (10–20 kHz). Systems such as JIGSAW operate in this mode with 32×32 Si GM-APDs. JIGSAW is a compact laser radar operating at 532 nm wavelength that has flown on a helicopter and demonstrated 3-D imagery through foliage [2]. The JIGSAW system required relatively low-timing jitter from the APD-to-ROIC detection process.

An example of an LC system is the Mars Laser Communications Demonstration (MLCD)—a recently canceled project for a 1.06-μm-wavelength link from Mars to Earth [3]. The demanding link budget for MLCD drove APD improvements in PDE, DCR, and reset time (T_R). It also led to a new architecture for a continuous-mode ROIC.

This paper describes recent advances in the performance of arrays of InP-based APDs that were integrated with a variety of CMOS ROICs specifically designed for imaging and time-tagging single-photon detections.

II. Detector Design and Figures of Merit

A. Detector Design

The completed detector depicted in Fig. 1(a) is a bonded stack of three semiconductors: a GaP microlens array, an InP APD array, and a Si CMOS ROIC that can time-stamp photon arrivals at each pixel. Not shown is the hermetic package that houses the semiconductor stack as well as a single- or double-stage thermoelectric cooler.

Similar detectors were originally developed for visible light using thinned arrays of planar Si GM-APDs that were epoxy bridge-bonded to a 32×32 ROIC [4]. Niclass *et al.* have

Manuscript received February 5, 2007; revised July 5, 2007. This work was supported by the National Aermautics and Space Administration.

The autors are with the Lincoln Laboratory, Massachusetts Institute of Technology, Lexington, MA 02420 USA (e-mail: simonv@ll.mit.edu).

Digital Object Identifier 10.1109/JSTQE.2007.904464

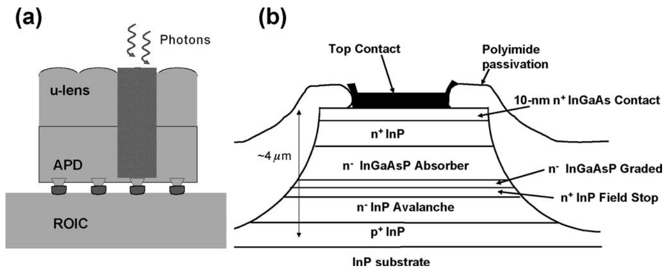

Fig. 1. (a) Bonded stack of a GaP microlens array epoxied to an InP APD array that is In bump-bonded to a Si CMOS ROIC. (b) Schematic of a 1.06-μm-wavelength InGaAsP–InP GM APD.

TABLE I
FIGURES OF MERIT FOR 1.06-μm-WAVELENGTH APDs

Parameter	Measured value	Comments
PDE	50%	20-um diameter mesa (15 um photoactive area), 5 V overbias.
DCR	20 kHz	5 V overbias, 25°C
T_R	~1 μs	25°C, on CMOS ROIC
L_0	0.09 dB	Self-blocking loss from dark counts

Measured values of key figures of merit at room temperature for 1.06 μm wavelength APDs using InGaAP absorber regions

reported a monolithic 32×32 detector comprising a 32×32 GM-APD array and associated CMOS readout electronics on the same die [5]. For SWIR applications, InP-based alloys make for GM-APDs with high detection efficiency, albeit with higher DCRs and longer reset times than for Si. Nonetheless, the availability of high-efficiency lasers and optical amplifiers at 1.06 and 1.55 μm wavelength has driven many system designers to InP-based GM-APDs. In addition, the 1.55 μm band has eye-safety benefits for certain LADAR and LC systems.

Our GM-APD arrays are well suited to applications that require relatively narrow field-of-view per pixel. The mesa-etched APDs depicted in Fig. 1(b) are patterned into 50- or 100-μm-pitch arrays and have low fill factor when used without microlenses. Details of the APD-mesa design are given in Section III. The GaP microlens array collects light from the focal plane with 70%–80% efficiency—dominated by optical loss in the seams between the lenslets. The APD-mesa diameter is minimized to reduce bulk contributions to the DCR. The minimum size is, however, constrained by the optical system feeding the complete detector stack. For f/10 optics and slower, 15-μm-diameter mesas preserve $>$70% coupling efficiency. Faster optical feeds (e.g., f/4) require larger mesas—30-μm-diameter mesas are compatible, for example, with the JIGSAW application. In general, many active optical systems use slow optics since transmitter power is precious and the receiver is often collecting light from a small illuminated target that subtends a small solid angle. A more detailed description of fabrication and packaging considerations is in Section IV.

Various array formats have been developed for both deep-space LCs and for LADARs. Smaller 1.06-μm-sensitive 8×8 arrays mated to an ROIC with automatic pixel reset were developed for the MLCD application. Recently, 1.55 μm 8×8 arrays were successfully operated with that ROIC. Larger 32×32 arrays operating at both 1.06 and 1.55 μm wavelengths are useful for LADAR systems like JIGSAW. Still in development are 32×32 ROICs with automatic pixel reset for LC, and 50-μm-pitch 128×32 and 256×64 ROICs with framed readouts for wider field-of-regard LADARs. The differences between framed ROICs and those with automatic pixel reset are described in Section VI.

B. Figures of Merit

Three interdependent figures of merit describe the utility of GM-APDs for most systems: PDE, DCR, and reset time (T_R).

The PDE is the product of three probabilistic processes: the quantum efficiency (QE) of creating a primary photoelectron–hole pair in the absorber, injection of the primary hole into the InP multiplier, and avalanche multiplication of the current into a sustainable cascade of electrons and holes. Often, the injection probability and multiplication probability are grouped together as the probability of avalanche (PA). In that case, $\mathrm{PDE} = \mathrm{QE} \times \mathrm{PA}$.

The DCR accounts for false firings of the APD due to dark carriers originating in either the absorber or multiplier and causing a GM breakdown. The PA associated with a primary dark carrier depends on where the carrier was created in the APD. Dark carriers created in the absorber account for most of the difference in DCR between 1.06 and 1.55 μm APDs.

After a GM-APD has detected either a photon event or a dark event, the likelihood of a subsequent dark count, or afterpulse, is elevated if the APD is immediately rearmed above its breakdown voltage. The reset time T_R is the minimum time the APD should be left disarmed—1–2 V below its breakdown voltage (60–70 V)—to avoid an afterpulse. This allows filled traps in the multiplier to empty through electric-field-assisted thermionic emission. The reset time depends on temperature and can limit the performance of LC systems receiving continuous-wave signals. A useful figure of merit for such systems is the zero-background blocking loss expressed in decibels:

$$L_0 \approx 10 \log_{10}(1 + \mathrm{DCR} \times T_R).$$

It describes the potential signal loss from the fraction of the array that is, on average, in reset mode due to a dark count. This blocking loss is less important for LADARs operating at pulse-repetition frequencies of 10–20 kHz or less since there is no need to reset pixels quickly.

Table I shows typical values of the figures of merit measured at room temperature for 1.06-μm-wavelength APDs. Examples of how these parameters depend on temperature and voltage overbias appear in Section III. Indeed, GM-APD structures are designed for a target temperature since the breakdown electric field strength is a strong function of temperature. Note that the reset times in Tables I and II were measured on ROICs and are therefore lower than those described in Section V.

Measured parameters for 1.55-μm-wavelength APDs are shown in Table II. Note that although the DCR is similar to the 1.06 μm case, it was achieved by designing a structure that fully

TABLE II
FIGURES OF MERIT FOR 1.55-μm-WAVELENGTH APDs

Parameter	Measured value	Comments
PDE	45%	20-um diameter mesa (15 um photoactive area), 5 V overbias.
DCR	20 kHz	5 V overbias, -30°C
T_R	~6 µs	-30°C, on CMOS ROIC
L_0	0.5 dB	Self-blocking loss from dark counts

Measured values of key figures of merit at −30 °C for 1.55-µm-wavelength APDs using InGaAsP absorber regions

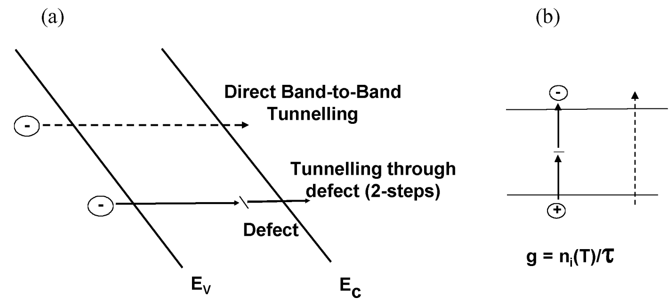

Fig. 2. Sources of primary dark carriers. (a) Defect-assisted band-to-band tunneling in the multiplier. (b) Defect-assisted thermal generation in the absorber.

depletes at approximately $-30\,^{\circ}$C. Operating at lower temperature reduces thermally generated dark carriers in the absorber, but increases the reset time. In 1.55 μm devices, the best combination of PDE and DCR occurs when the multiplier field strength just approaches the breakdown field when the absorber is barely depleted. This minimizes field-assisted dark-carrier generation in the absorber while preserving a useful avalanche probability in the multiplier, as will be discussed later.

III. Epitaxial Layer Design and Modeling

Early work on photon counting at SWIR wavelengths used high-quality linear-mode APDs optimized for fiber-optic receivers. GM operation was then demonstrated by cooling these devices and applying short voltage-bias pulses. More recent work focused on improving the design of APDs for photon counting [6], [7].

This section describes how separate absorber and multiplier (SAM) APDs can be optimized for GM operation at both 1.06 and 1.55 μm wavelengths. A more detailed explanation of the design calculations for 1.06 μm APDs based on experimentally extracted parameters is also available [8].

A. 1.06 μm APDs

The APD structure for 1.06 μm operation is shown schematically in Fig. 1(b). It is an n-type on p-type mesa structure with a sidewall profile designed to minimize edge breakdown of the junction. It has a separate InGaAsP absorber, a bandgap-graded layer, a doped field stop or charge layer, and an avalanche or multiplier layer. The anode contact is made to the bottom p^+ layer. Most of our arrays are fabricated on low-loss n^- and n^+ substrates, with the n^+ substrates having much lower etch-pit densities.

In 1.06 μm APDs, sources of dark counts are electric-field-assisted tunneling and thermal generation currents in the different sections of the device. Fig. 2 depicts these two mechanisms for generating primary dark carriers. Thermal generation rates, even in these direct gap semiconductors, are dominated by defects and depend on the crystalline quality of the material. The material quality can be associated with a carrier lifetime τ. Then, the thermal generation rate is simply n_i/τ, where n_i is the intrinsic carrier concentration of the material. This mechanism is most important in the absorber, since n_i depends on both its bandgap and temperature. In the multiplier, both direct band-to-band tunneling as well as indirect tunneling through defect states in the bandgap are important. In our devices, defect-assisted tunneling in the InP avalanche region is much higher than direct band-to-band tunneling and is the dominant source of DCR in 1.06 μm devices.

A dark primary carrier can lead to a dark count only if it is generated in or injected into the multiplier and starts a sustainable avalanche. The PA is, therefore, a key concept for calculating both DCR and PDE. Since each ionization event is probabilistic, the likelihood of an actual breakdown occurring due to a single electron–hole pair will also be probabilistic. PA will increase with overbias, with its rate of increase dependent on the ratio of the ionization coefficients for holes and electrons. PA will also depend on the position where an electron–hole pair is generated. Since the ionization coefficient for holes is greater than that of electrons, the PA will be higher for holes injected into the avalanche region from the absorber than for electrons injected from the p^+-region. For electron–hole pairs generated in the multiplier itself, the PA will depend on position and will fall between that of pure hole and pure electron injection.

The PA versus voltage for holes injected from the absorber for different avalanche thicknesses is shown in Fig. 3. The absorber thickness in all cases is 1.5 μm and the field stop thickness was chosen so that the absorber would be fully depleted at breakdown. The points where the PA curves go to zero indicate the calculated breakdown voltage. The insert shows PA versus overbias and indicates that PA does not strongly depend on avalanche thickness. In InP, breakdown voltage decreases by about 1 V for every 10 K decrease in temperature. PA increases slightly with decreasing temperature due to an increase in the ionization coefficients ratio at lower fields. More information about the ionization coefficients used in these calculations has been published [8].

The DCR calculations account for both dark carrier generation and for the PA. Fig. 4 shows such calculations for our 1.06 μm APDs for various multiplier widths and as functions of overbias and temperature.

The devices whose DCRs are shown in Fig. 4(a) had a 1.5-μm-thick absorber with a bandgap of $E_g \approx 1.05$ eV ($\lambda_g \approx$ 1.18 μm). All of the fits were carried out using the same density

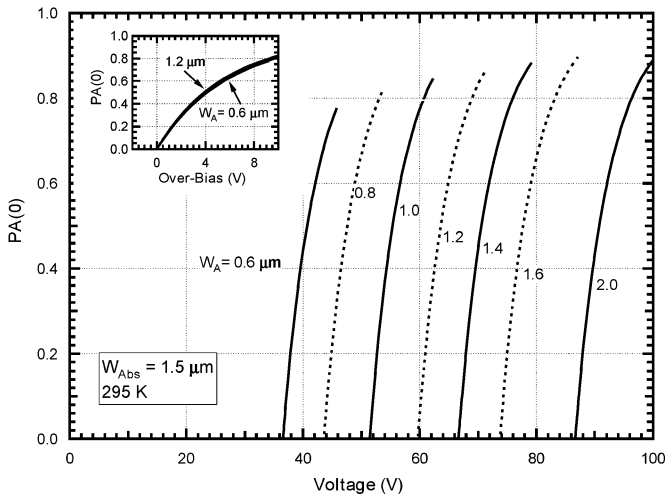

Fig. 3. PA given hole injection through the field stop region into the multiplier. $W_{\rm A}$ refers to different thicknesses of the multiplier region. (Inset) PA as a function of overbias beyond the steady-state breakdown voltage of the APD.

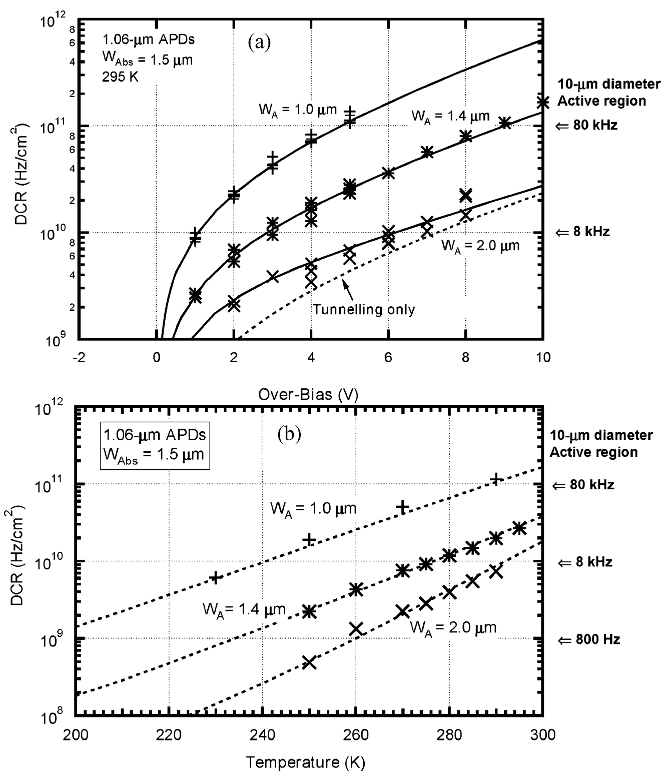

Fig. 4. Numerical fits to measured DCR in 1.06-μm-wavelength APDs. (a) Fits to the DCR per unit area of 1.06 μm APDs with 1.0, 1.4, and 2.0 μm avalanche regions. (b) Fits versus junction temperature. DCRs for a typical APD with 10-μm-diameter photoactive area are indicated on the rightmost range axis.

of defects for tunneling current in the avalanche region for all devices and a lifetime τ of 40 μs in the absorber. This lifetime is quite large indicating high-quality material. Also shown is the DCR attributable only to tunneling in the avalanche region for the devices with 2.0 μm avalanche regions to give some idea of the portion of DCR due to generation current in the absorber. As material quality improves, DCR will decrease further due to fewer defects through which tunneling can take place. In fact, many recent devices have shown DCRs a factor of 2 lower than shown here due to further improvements in material quality.

Since the breakdown voltage decreases with decreasing temperature, the DCR even in devices dominated by tunneling in the avalanche region decreases significantly as the temperature of operation is reduced [see Fig. 4(b)]. The DCR per unit area versus temperature of several devices with different avalanche layer thicknesses at 4 V overbias is shown in this figure. These devices are from different growth runs than the devices shown in Fig. 4(a). In particular, the device with the 1.0-μm-thick avalanche region comes from an older wafer and has a larger DCR than the comparable devices shown earlier. The room-temperature DCRs on the other devices are also slightly higher (20%–30%) than the average DCR fit mentioned before, indicative of run-to-run and device-to-device variation. Nonetheless, the fit to the temperature dependence is quite good.

The PDE can be thought of as the probability of a photon being absorbed and creating an electron–hole pair times the probability that this electron–hole pair will cause a sustained avalanche. If photons were only absorbed in the InGaAsP absorber region, this would be essentially the QE of the diode (i.e., with only unity gain) times the PA for hole injection into the avalanche region. For 1.06-μm-wavelength devices, however, electron–hole pair generation via electroabsorption in the high-field avalanche region must also be taken into account. Electron–hole pairs generated in the avalanche region via electroabsorption have a lower position-dependent PA than those generated in the absorber, as discussed earlier.

In addition, reflections and any photons lost to free-carrier absorption before reaching the active region must also be taken into account. Although free carrier absorption takes place in all of the doped layers, it is generally only of significance in our back-illuminated devices with heavily doped substrates.

The PDE versus overbias calculations for a back-illuminated 1.06 μm device with an n^+ substrate, a 1.0-μm-thick avalanche region and a 1.5-μm-thick absorber region at temperature 273 K (0 °C) is shown in Fig. 5, along with data taken on a back-illuminated device with an n^+ substrate. The n^+ substrate had a measured loss of 7 cm^{-1} at 1.06 μm. To increase PDE, an undoped or lightly doped substrate can be used to virtually eliminate the substrate loss. In back-illuminated devices, the PDE can be further increased by replacing the top cathode contact with a highly reflective metal, resulting in essentially a double pass through the absorber. This is preferable to increasing the absorber thickness since this would result in lower fields in the avalanche region at any overbias, effectively decreasing PA and PDE. In fact, with a 90% reflector, optimum PDE can actually be obtained with a thinner absorber.

B. 1.55 μm APDs

Schematically, the design of a GM-APD for 1.55 μm wavelength follows that shown in Fig. 1(b), but with the quaternary absorber replaced with $In_{0.53}Ga_{0.47}As$. The reduced bandgap of

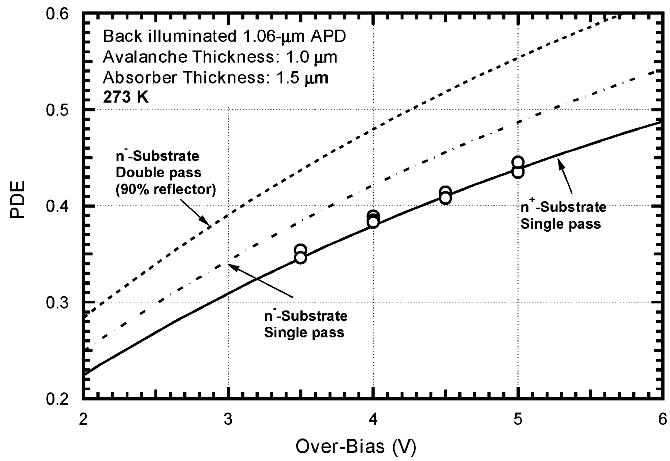

Fig. 5. Calculations (solid line) and comparison to measured PDE on an n^+ substrate (circles). Increases in PDE are attainable by using lower loss n^- substrates and by using a reflective electrical contact at the cathode (dashed lines).

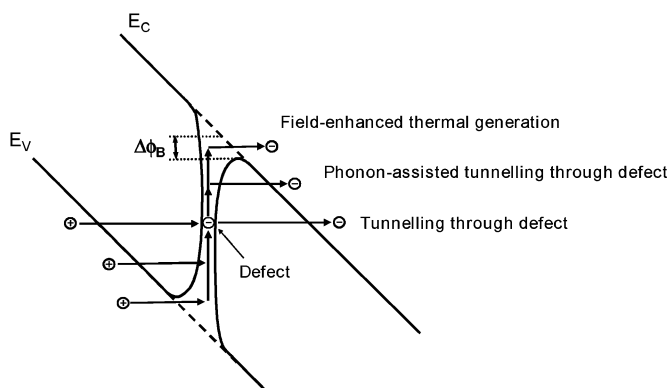

Fig. 6. Mechanisms for generating primary dark carriers in the InGaAs absorber.

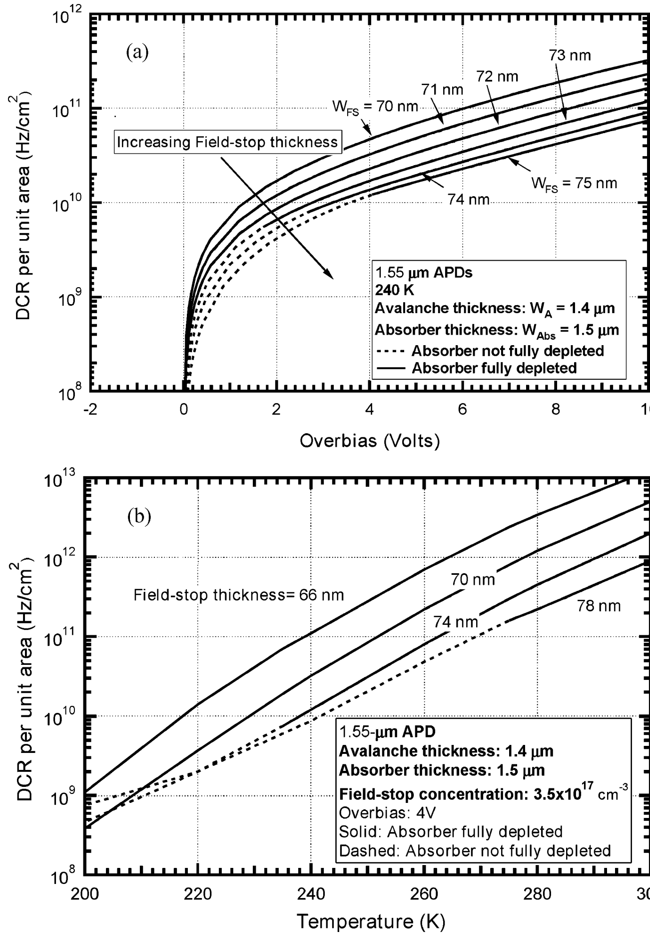

Fig. 7. Calculated DCR for 1.55-μm GM-APDs. (a) DCR versus overbias voltage. (b) DCR versus junction temperature.

the absorber in 1.55 μm APDs, however, increases the difficulty of matching the performance of 1.06 μm APDs. Fig. 6 illustrates three different mechanisms for generating primary dark carriers in the InGaAs absorber.

In calculating the DCR due to carriers generated in InGaAs, we considered generation through defects, which is enhanced by high fields (Poole–Frenkel effect), tunneling, both direct tunneling through defects, and importantly, phonon-assisted tunneling through defects. Field-enhanced generation and phonon-assisted tunneling were negligible in the 1.06 μm APDs because of the larger absorber bandgap and the dominance of tunneling in the multiplier for those devices. These mechanisms are, however, a main source of dark current in 1.55 μm APDs.

Since the InGaAs dark-current mechanisms are extremely field dependent, it is essential to minimize the field in the absorber at the desired operating temperature and overbias. This can be done by carefully adjusting the charge in the field stop layer. Since the resulting DCR is also very sensitive to the exact field in the absorber, the accuracies of these 1.55 μm device calculations are not expected to be as precise as those for the 1.06 μm devices.

Calculated curves of DCR versus overbias at 240 K are shown in Fig. 7(a) for several different field stop thicknesses. All of the devices had a 1.4-μm-thick InP avalanche region, a 0.1 μm bandgap-graded region, and a 1.5 μm InGaAs absorber region. The field stop doping was 3.5×10^{17} cm^{-3}. For operation with 4–5 V of overbias, optimal field stop thicknesses are 74–75 nm. The solid lines in the figure indicate fully depleted absorbers, while the dashed lines indicate partially depleted absorbers. Note that the best performance occurs at voltages just beyond the point of depletion. For thicker field stops, the absorber will not be fully depleted and the PDE will be degraded. For thinner field stops, field-enhanced generation in the absorber degrades the DCR.

At 240 K, tunneling in the avalanche region is no longer negligible for 1.55 μm APDs. Its effect can be seen in Fig. 7(b) for the devices with the thicker field stops (smaller decrease in DCR with temperature), where the absorber is not fully depleted at breakdown.

Fig. 7(b) shows the calculated DCR at 4 V overbias for 1.55 μm devices with several different field stop thicknesses. At higher temperatures, the DCR decreases substantially as the field stop thickness increases due to a decrease in the electric field in the absorber, resulting in decreased field-enhanced

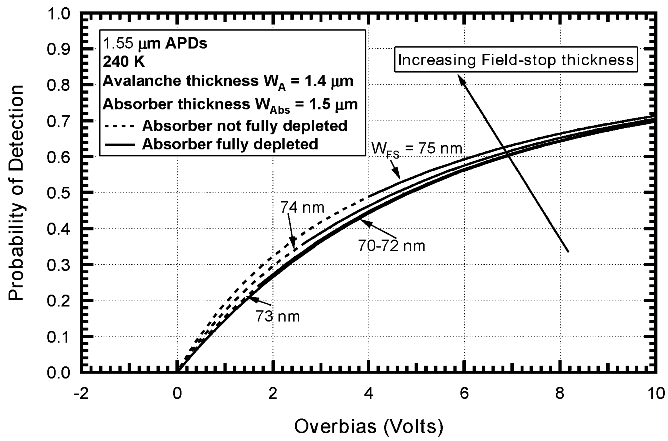

Fig. 8. Calculated PDE for 1.55 μm GM-APDs with various field stop thicknesses.

generation and phonon-assisted tunneling. To efficiently collect carriers and minimize timing jitter, the absorber should be fully depleted at the operating temperature and overbias (typically 4–5 V with our CMOS ROICs). Again, the dashed part of the curve indicates where the depletion region has not yet moved through the absorber. Therefore, there is an optimal field stop thickness for certain operating temperature ranges. If it is desired to operate around 280 K, an optimal field stop thickness is around 78 nm. At 240 K, the optimum is 74 nm; at 200 K, it is 70 nm.

The process for calculating PDE for 1.55 μm APDs is similar to that used for 1.06 μm devices. At 1.55 μm, electroabsorption in the avalanche region is negligible. The PDE is determined entirely by absorption in the InGaAs absorber region and by the PA for holes injected into the avalanche region. The calculated PDE versus overbias for back-illuminated 1.55 μm APDs at 240 K with different field stop thicknesses is shown in Fig. 8. The devices have the same layer thicknesses and field stop doping as those in Fig. 7. An undoped substrate and a 90% reflector for the cathode contact for double-pass operation are assumed. Although the absorption coefficient decreases with decreasing temperature, Fig. 8 indicates PDEs in the 50% range can be obtained at 4–5 V overbias at 240 K. The PDE is independent of field stop thickness when the absorber is fully depleted at breakdown. When the absorber is no longer fully depleted at breakdown, there is an enhancement in PDE due to a higher field in the avalanche region at any overbias (higher PA).

IV. Fabrication and Reliability

A. Epitaxial Layer Growth

The APD structures are grown by organometallic vapor phase epitaxy (OMVPE) on (1 0 0) InP substrates. We have used p^+, n^+, and n^- substrates. A two-step p^+ InP layer is grown first to serve as the p-side (anode) of the junction. The lower part is 1.5 μm thick and has a Zn doping of 1.6×10^{18} cm^{-3}, while the upper part is 0.5 μm thick and has a doping of 8×10^{17} cm^{-3}. The nominally undoped InP avalanche region of thickness W_{A} (0.8–2.0 μm) is grown next and has an n-type concentration $\approx 10^{15}$ cm^{-3}. This is followed by a heavily Si-doped n^+-InP ($N_{\mathrm{FS}} = 3.5$–7.0×10^{17} cm^{-3}) field stop layer of thickness W_{FS}. The $N_{\mathrm{FS}} \times W_{\mathrm{FS}}$ product is chosen so that, first, the absorber layer is fully depleted at the overbias and temperature of operation, and second, the maximum field in the absorber is below a maximum value at the operating conditions. In 1.06 μm devices, the maximum field in the absorber is usually kept below 1×10^5 V/cm, while in 1.55 μm devices, it is kept as small as possible (low 10^4 V/cm), as discussed in Section III. The first criterion assures that photocarriers generated anywhere in the absorber are swept quickly to the avalanche region reducing jitter. The second criterion minimizes any field-enhanced dark current in the absorber.

A compositionally graded InGaAsP layer is then grown to facilitate the injection of photogenerated holes from the absorber into the avalanche region. The graded layer is 50 and 100 nm thickness for 1.06 and 1.55 μm APDs, respectively. The nominally undoped InGaAsP or InGaAs absorber ($n < 10^{15}$ cm^{-3}) of thickness W_{Abs} (typically 1.5 μm) is then grown. This is followed by an n^+ InP layer and a 10-nm-thick n^+ InGaAs contact layer.

Our hypothesis is that the dominant defect for dark carriers originating in the avalanche region is the phosphorous vacancy (V_{P}). Experiments were performed to look at the effect of growth parameters on DCR. Growth temperature, growth rate, and V/III ratio should all have some influence on the materials properties [9]. We isolated the effect of the InP multiplier by using dummy APDs with InP absorbers and with controlled changes in growth parameters. The InP dummy APDs were grown at temperatures of 650, 625, and 600 °C. The effect of decreasing the temperature to 625 °C resulted in ~44% decrease in DCR. Further decrease of the growth temperature yielded no statistically significant improvement in DCR and resulted in poorer surface morphology. Thus, a growth temperature of 625 °C was chosen.

As discussed by Donnelly *et al.* [8], the DCR observed in these 1.06 μm APDs is one to two orders of magnitude higher than that expected from band-to-band tunneling alone in the high-field InP avalanche region. Dark counts are, therefore, dominated by defect-assisted tunneling through a defect state located somewhere in the InP bandgap. Fourier-transform deep-level transient spectroscopy (FT-DLTS) results are shown in Fig. 9 for a 3-μm-thick not-intentionally-doped (nid) InP layer. This layer was grown under identical conditions to the avalanche region. The DLTS data indicate a defect state ~0.42 eV below the conduction band edge. A defect state at this energy level has been widely reported in InP [10], and is likely related to phosphorus vacancies. The energy level of a neutral phosphorus vacancy calculated from first principles and including the effects of lattice distortion around the defect [11] is in good agreement with the DLTS results mentioned before. It is also noted that this energy level is similar to that ($E_{\mathrm{C}} - 0.34$ eV) extracted from a fit of DCR versus overbias for a range of APD geometries using a comprehensive model [8]. Since the phosphorus vacancy is calculated [11] to have the lowest formation energy of various native defects under a wide range of doping levels and V/III ratios, it would not be surprising if it were present in the avalanche region.

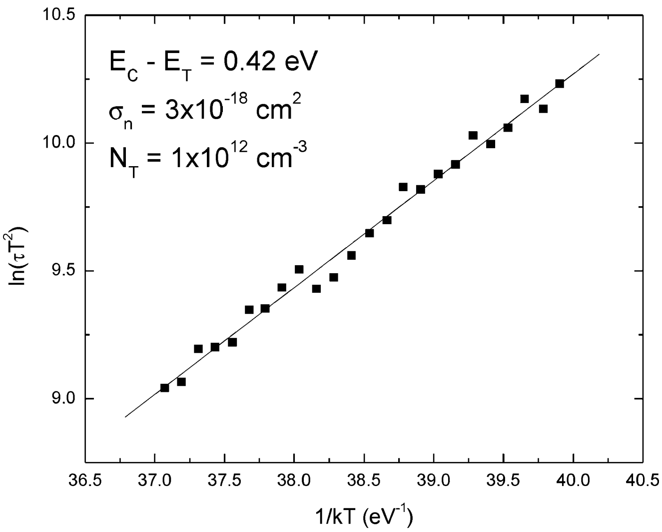

Fig. 9. FT-DLTS results for nid InP, plotting carrier emission rate versus inverse thermal energy, indicating a single dominant defect level located 0.42 eV below E_{C}.

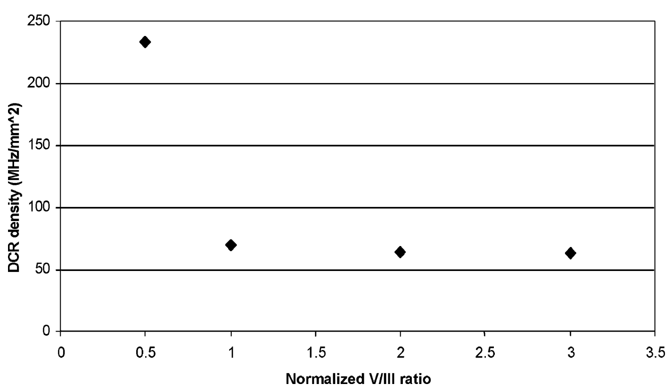

Fig. 10. Measured DCR density for InP-absorber dummy APDs versus normalized V/III ratio during OMVPE growth.

We also expect the V/III ratio to affect the V_{P} defect concentration. The energy of formation of a V_{P} defect should increase with increasing V/III ratio, thereby decreasing its concentration. Other researchers have shown that mobility and photoluminescence intensity increase, and then, saturate with increasing V/III ratio [12]. This is thought to be a combination of several effects, including the reduction of V_{P} concentration. Additional InP dummy APDs were grown with the V/III ratio changed only during growth of the avalanche region. The V/III ratio was varied from 0.5 to 3 times its normal value of a 110:1 flow-rate ratio for the phosphine to trimethylindium precursors. Fig. 10 shows the results of DCR measurements versus normalized V/III ratio. Only modest improvements were gained at higher V/III, but a significant increase in DCR ($\sim$3.2 $\times$) was observed for a normalized V/III ratio of 0.5. This result indicates that the current V/III ratio is nearly optimal for high-quality material.

B. Mesa-Diode Fabrication

The GM-APD mesa fabrication isolates the individual pixels of the array but must not introduce defects or current paths that can degrade the performance. Mesa etching also isolates the devices optically and reduces crosstalk. However, the interface of the semiconductor mesa with a dielectric passivation layer potentially introduces a surface layer that can degrade the performance of the device over time. The mesa-passivation material is, therefore, a critical part of the device design.

Other workers have demonstrated reliable planar APDs operating in either GM or linear mode. Planar APDs typically use lithographically controlled Zn diffusion to define arrays of APDs, and therefore, avoid etched sidewalls altogether. See [13] and [14] for two recent descriptions of planar GM-APDs.

The array fabrication sequence begins by etching completely through the active layers of the device to define mesas. The etch is either a nonselective wet etch or an inductively coupled plasma reactive ion etch (ICP-RIE) followed by a brief wet cleanup etch to remove ion damage. Large array fabrication requires the dry etch process since it is more spatially uniform across the wafer than the deep wet etch. Following mesa etching, passivation is applied and ohmic contacts are made to the top of the mesa (cathode). For top-illuminated test devices, an annular contact is used. For back-illuminated devices that mate to ROICs, a disk-shaped contact is used. Anode contacts are either made to the back of the substrate or on the top to the etched p^+ anode layer. For back illumination, wafers are thinned to 150 μm and antireflection coatings applied.

Various passivation materials have been utilized including polyimide, polyimide overcoated with silicon nitride or silicon dioxide, bisbenzocyclotene (BCB), hydrogensilsesquioxanes (HSQ), pyrolytic silicon dioxide, and regrown InP. Of these, the current focus is on polyimide coated with silicon nitride or silicon dioxide. Regrown InP passivation is also being investigated. The best initial performance with stable aging characteristics has been obtained with polyimide coated with silicon nitride. The polyimide coats the mesa and passivates the semiconductor surface and the nitride fills in any microcracking and protects the polyimide from low levels of moisture. Regrown InP may be the best passivation since these devices have shown the most stability with time [15]. Initial results, however, indicate that the initial DCRs of these APDs are much higher. The DCRs on the regrown InP APDs appear to be dominated by an edge leakage effect rather than the bulk effect that dominates devices passivated by polyimide. This is evidenced by the scaling of the DCR with device perimeter rather than the area. Further effort is underway to improve the mesa/regrowth interface to remove the defects that may be causing the high DCR.

Although GM-APD arrays on ROICs have operated reliably in demonstration systems, DCR increases during operation have been noted while testing some APDs with bench electronics. Hence, understanding the degradation of these devices and improving their reliability through design changes or screening is critical. Similar APDs have been operated in linear mode and shown to be stable for many thousands of hours for

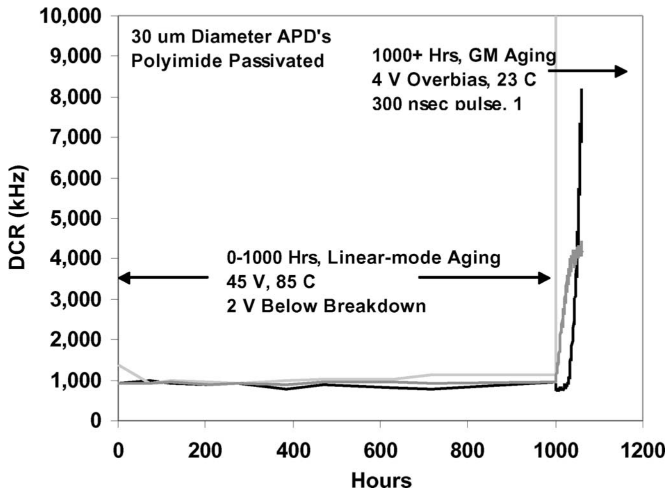

Fig. 11. Aging of several GM-APDs in linear mode (below breakdown) and in GM (pulsed over breakdown).

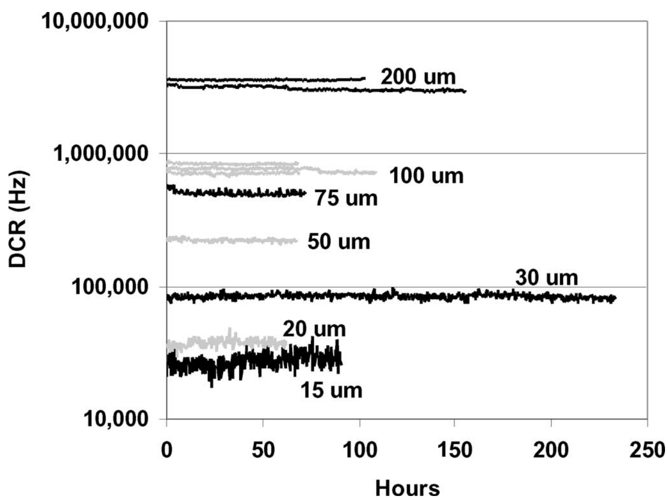

Fig. 12. GM aging of many APDs passivated with polyimide coated with silicon nitride. The size indicated is the diameter of the device and the aging conditions are the same as those in Fig. 11. The small variations in DCR are mostly statistical and are typical for the thousands of APDs measured in this apparatus.

telecommunication applications [15]–[17]. However, operation in GM appears to be more stressful to the devices. Fig. 11 shows the DCR of APDs aged just below the breakdown for 1000 h with no degradation. But when these same devices are pulsed 4 V over breakdown, they show degradation within a few hours of GM operation [18]. These devices were passivated with only polyimide. Fig. 12 shows GM aging data on several APDs of different diameter passivated with polyimide coated with silicon nitride. To date, these devices have shown several hundreds of hours of stability indicating that devices can be designed to be more resilient in GM operation.

C. Microlens Alignment and Packaging

In most LADAR and LC applications, cross-range resolution is important and the receiver's optical system locates its image plane at the plane of the microlenses. A given microlens focuses an image pixel into the APD absorber—transforming its airy disk into a pupil-plane image. Therefore, the optical intensity profile on the APD depends on the f/# and feed type (e.g., Cassegrain with a central obstruction). Nonetheless, useful estimates of the fill factor for f/10 systems and slower can be made by assuming plane-wave illumination at the image plane.

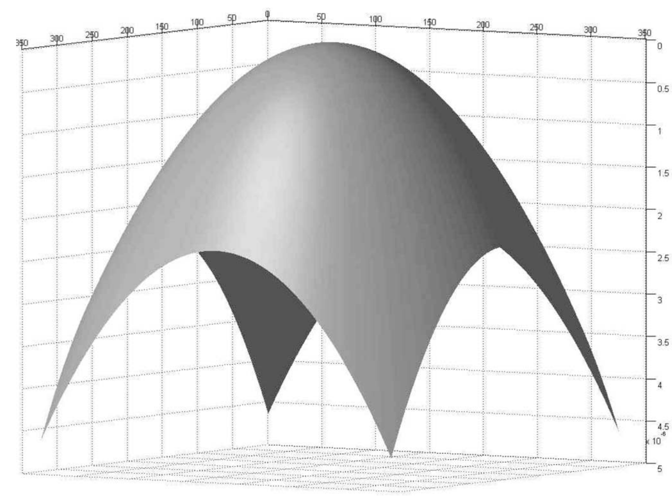

Fig. 13. Measured profile of a GaP microlens element from a 100-μm-pitch array.

Fig. 13 shows the measured profile of a GaP lenslet from a microlens array with a pitch of 100 μm [19]. The lens was profiled using a white-light interferometer [20]. Utilizing the profile data from the interferometer, we are able to predict the spot size, radius of curvature, and encircled energy as a function of the diameter of the APD.

The encircled energy can be estimated using either commercial ray-tracing software or by computing the Fresnel-propagation solution. Both methods gave similar results for the encircled energy, although the Fresnel-propagation code should more accurately account for diffraction effects when the system is out of focus and is near-diffraction limited. A prediction for encircled energy from the Fresnel-propagation method is shown in Fig. 14.

Microlens arrays with favorable predictions for encircled energy are then thinned to $\sim$150 μm thickness and antireflection coated for either 1.06 or 1.55 μm, and are paired with an APD array of appropriate thickness. The APD and microlens arrays are placed into a custom alignment system that allows for precise six-axis alignment of the microlens to the APD array. The alignment is accomplished utilizing an error signal from a collimated input beam that passes through the microlens array to alignment diodes located in the four corners of the APD array. The alignment diodes are GM-APD structures that are bump-bonded to the ROIC and directly connected to wire bond pads. With a modest reverse-bias voltage applied to the alignment diodes, the photocurrent can be monitored as the arrays are aligned. This is accomplished while monitoring two of the alignment APDs at opposite corners and adjusting rotation and translation until concurrent peak-photocurrent values occur. Fig. 15 shows how

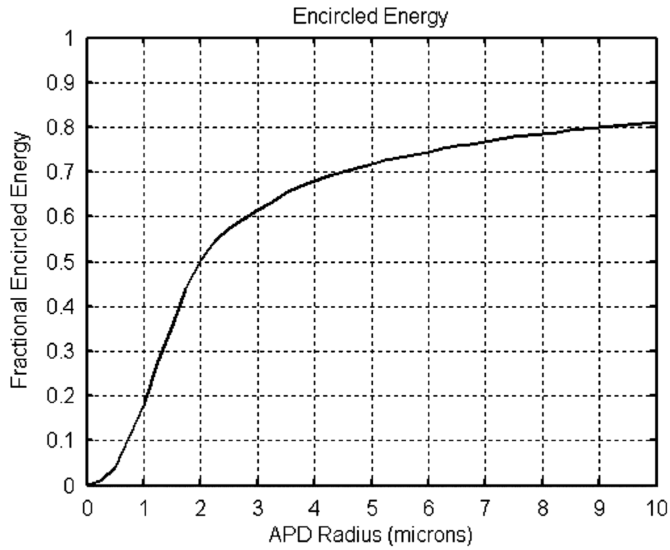

Fig. 14. Prediction of encircled energy versus APD photoactive radius, based on the measured surface profile shown in Fig. 13.

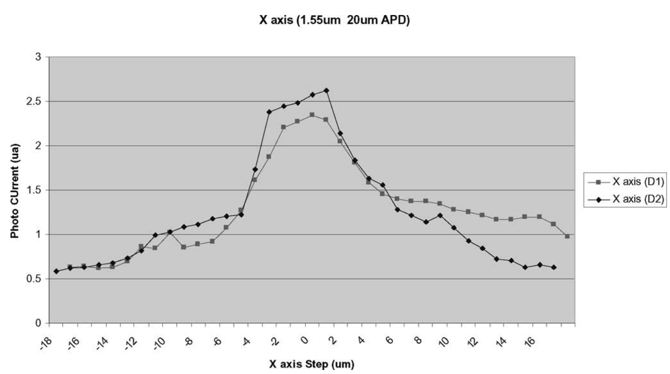

Fig. 15. Measured photocurrent from two optical alignment diodes in the corners of a 32×32 InP APD array. This is used as an error signal while aligning and attaching the GaP microlens array.

the peaks occur at the same X-axis location once rotational alignment is achieved.

Once the maximum photocurrent is realized in the X-, Y-, Z-, and θ-axis in at least two of the alignment diodes, the positional alignment is complete. This method of using the diodes actively during alignment reduces alignment errors through the use of the actual optical path. It results in near-perfect alignment for maximizing the optical efficiency of the APD array. Adhesive is then applied between the microlens and APD arrays and allowed to cure. The photocurrent is monitored during the entire process to ensure accuracy.

V. Measured Detector Performance

Before packaging a GM-APD array with an ROIC and microlenses, we perform wafer and die-level measurements on the InP array. Next, we show representative data on PDE, timing jitter, breakdown-voltage uniformity, and reset time for both 1.06 and 1.55 μm devices.

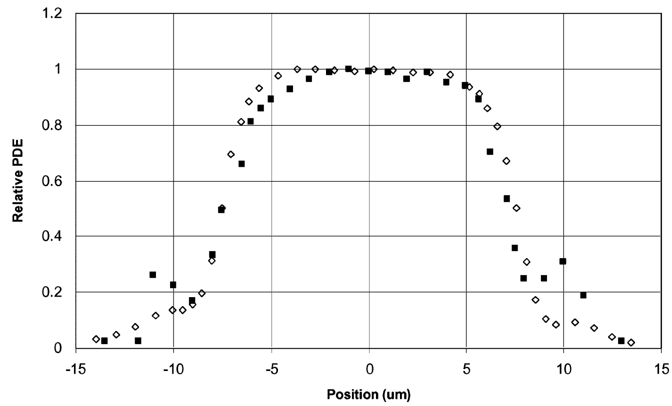

Fig. 16. Normalized raster scans through the center of a 1.06 μm (squares) and a 1.55 μm (diamonds) GM-APD. Although the diameter of the mesa-etched APD is 20 μm, the photoactive diameter is $\sim$15 μm, as measured by the FWHM.

A. Photon Detection Efficiency

The PDE was measured with a raster method for back-illuminated GM-APDs not attached to an ROIC. A direct-modulated laser emitted 1.06 μm pulses of 100 ps width that were attenuated and focused through the InP substrate into the InGaAsP absorber. A microscope objective with numerical aperture 0.47 was used at both wavelengths. The measured full-width at half-maximum (FWHM) spot diameter was $\sim$2.8 μm at 1.06 μm wavelength. The voltage overbias was gated with a pulse generator and the intensity was adjusted to ensure Poisson photon-arrival statistics. Dauler *et al.* previously described the PDE measurement setup in more detail [21].

Fig. 16 shows the relative PDE cross sections for a 20-μm-diameter 1.06 μm APD at 295 K and for a 20-μm-diameter 1.55 μm APD at 250 K. The photoactive diameter of the device is always smaller than the physical diameter of the mesa. The photoactive diameters are comparable for both wavelengths—about 15 μm. Each PDE cross section is normalized to itself. The peak values of PDE are 55% and 50% for 1.06 and 1.55 μm APDs, respectively. When averaged over a diameter useful for microlens coupling (10–15 μm), the effective PDE is approximately that given in Tables I and II.

Measured PDE values for the 1.55 μm APD are shown in Fig. 17. Also shown are calculated PDE values using the models for QE and PA described in Section III-B. Here, the calculated PDE is reduced from the predictions of Fig. 8 due to loss in the n^+-substrate on which this device was fabricated and a reduced top-contact reflectivity. There is good agreement, however, between the predicted increase in PDE with overbias and measured results for a 1.55 μm APD.

B. Dark Count Rate

The DCR is typically measured using a gated voltage source to briefly overbias the APD. Either probes or wire bonds are connected to the cathode of the samples under test. A nearby ballast resistor of 50 kΩ limits current through the device until the device is turned off at the end of the gate. In other test setups, we use active circuits to more rapidly quench the avalanche and

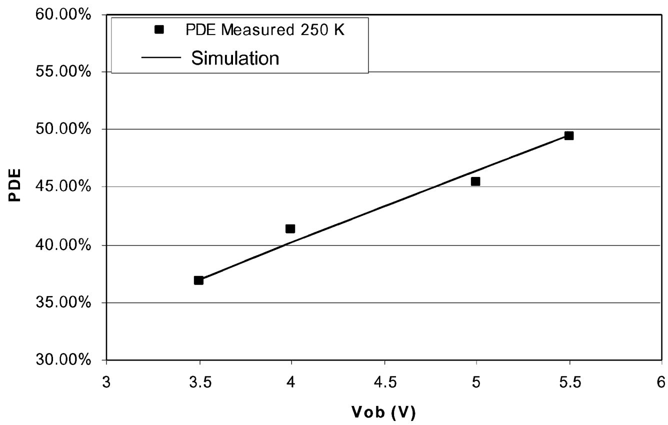

Fig. 17. Measured PDE at 250 K versus overbias for a back-illuminated 20-μm-diameter 1.55 μm APD using a 1.55 μm pulsed diode laser for excitation.

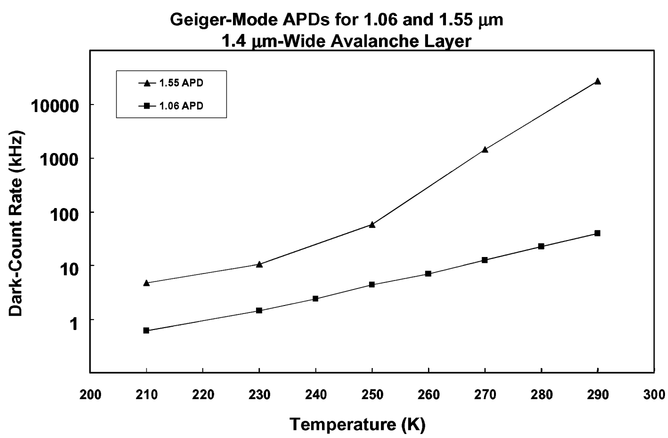

Fig. 18. DCR for 1.55- and 1.06-μm-wavelength GM-APDs with 4 V of overbias and 30-μm-diameter mesas.

minimize the amount of charge flow—which can reduce the reset time.

Fig. 18 shows the temperature dependence of the DCR for 30-μm-diameter GM-APDs designed for 1.06- and 1.55-μm-wavelength light. At all temperatures shown, the DCR of the 1.06 μm APD is dominated by defect-assisted tunneling in the InP avalanche region. This mechanism acts as a baseline dark-count contributor for the 1.55 μm APD, with thermal generation and tunneling in the InGaAs absorber dominating at temperatures above ~250 K.

Fig. 19 shows the measured timing jitter for 1.06 and 1.55 μm APDs at 4 V overbias. The absorber and avalanche thicknesses were 1.5 and 1.4 μm, respectively. Measurements indicate that 300–400 ps of timing jitter is typical in these APDs. Optical pulses with 100 ps width were used for the measurement. The jitter is more symmetrical than predicted by a simple model, indicating that the circuit may be contributing to the measured jitter.

The pixel-to-pixel breakdown voltage must be uniform enough to allow each APD in an array to efficiently detect photons and effectively trigger the timing circuit when the full array is biased with a single voltage. Typically, that requires an array to have less than about 1.5 V of variation in breakdown voltage. Shown in Fig. 20 is a map of the breakdown voltage

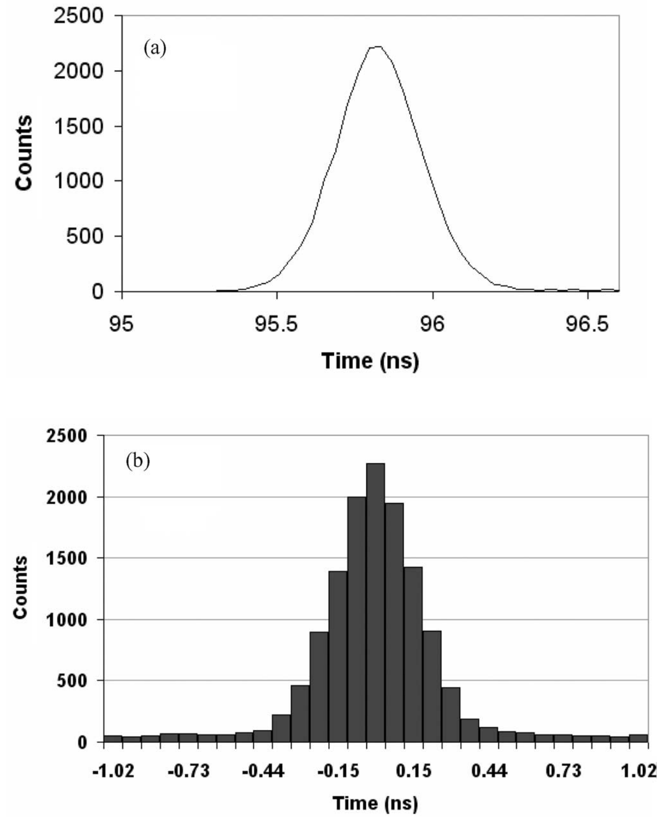

Fig. 19. GM-APD timing jitter measured on probed devices in gated-mode operation at room temperature. (a) 1.06 μm APD at 4 V of overbias. (b) 1.55 μm APD at 4 V of overbias.

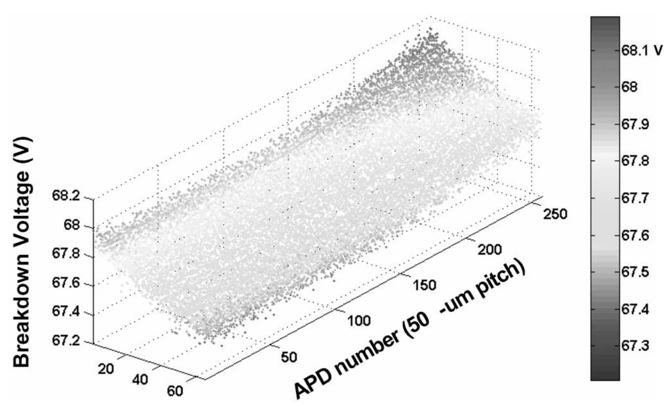

Fig. 20. Breakdown uniformity measured on a probe station for a 1.06-μm-wavelength 256×64 array.

measured with an automated probing system for a 256×64 array of 50-μm-pitch GM-APDs designed for 1.06 μm wavelength. The peak-to-peak variation in breakdown voltage for this array is ~1 V.

C. Reset Time

The reset time T_R is the length of time the APD must stay in its disarmed state after having fired. Leftover carriers from the previous avalanche breakdown that are trapped in the APD

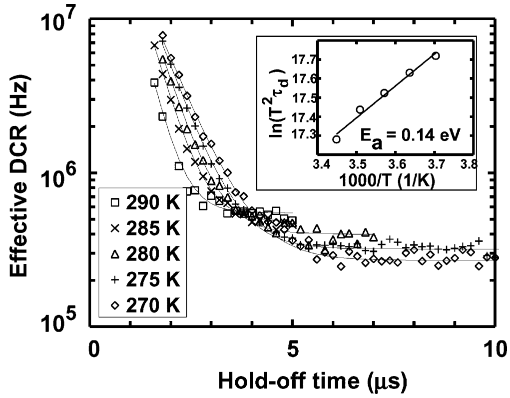

Fig. 21. Effective DCR versus hold-off time for a 1.06 μm APD. The APD fired and filled traps at zero time.

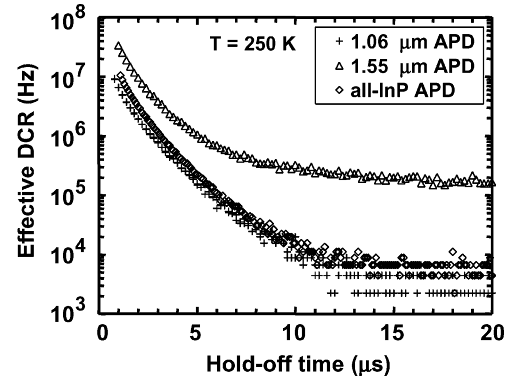

Fig. 22. Comparison of afterpulsing measurements on 1.06 and 1.55 μm GM-APDs. Also shown is an all-InP dummy APD, which overlaps the 1.06 μm APD results.

can then escape harmlessly, avoiding another dark count or afterpulse.

During the breakdown event, a large amount of charge flows through the APD. The amount of charge depends on the operating conditions and embedding environment of the APD. For an APD bump-bonded to a CMOS ROIC (a low-stray-capacitance environment) operated in actively quenched mode, the GM breakdown charge can be less than 0.5 pC (3×10^6 electrons), while a probed or wire-bonded APD operated in gated mode might conduct more than 2 nC (1.2×10^{10} electrons) during a 500 ns overbias gate. The reset times in Tables I and II are those for operation on ROICs where the number of filled traps is at least 10 times lower than for wire-bonded APDs. After the avalanche is quenched, the trapped carriers thermally depopulate. By measuring the depopulation rate as a function of APD temperature, the activation energy of the trap state can be estimated. Near room temperature (290 K), the depopulation rate can be described by a single time constant, implying that there is a dominant trap state. This is true for both 1.06 and 1.55 μm APDs that share a common InP multiplier design. The trap depopulation means that the Poisson rate parameter describing the count rate of the APD is time dependent:

$$\lambda(t) = R_{\mathrm{dark}} + R_\gamma + R_s + \mathrm{PA} \times \frac{N_{\mathrm{ft}}}{\tau_d} \exp\left(-\frac{t + t_{\mathrm{ho}}}{\tau_d}\right)$$

where R_{dark} is the DCR, R_γ is the optical background rate, R_s is the signal photon rate, PA is the avalanche probability, N_{ft} is the number of filled traps, τ_d is the detrapping time, t is the time after rearming, and t_{ho} is the hold-off time (i.e., the dead time since the last avalanche was quenched).

Fig. 21 shows data from a double-gated afterpulse measurement during which a laser forces the APD to fire during the first gate (driving approximately 5 to 20 pC through the APD), and then, the effective DCR is measured in a second gate at some hold-off time after the first gate. Each curve is fit with a single exponential decay time constant τ_d and number of filled traps N_{ft}. We assume that the trap lifetime (τ_d) is

$$\tau_d = \frac{1}{\sigma \nu N} \exp\left(\frac{E_a}{kT}\right)$$

where σ is the trap cross section, v is the free-carrier thermal velocity, N is the density of states of the relative band, and E_a the activation energy. Assuming temperature dependencies of $v \,\alpha\, T^{1/2}$ and $N \,\alpha\, T^{3/2}$, the Arrhenius relationship is obtained by plotting ln($T^2\tau_d$) versus 1000/T, as shown in the inset of Fig. 21. The linear fit to the data yields an activation energy of 0.14 eV. At 290 K, the detrapping time is approximately 0.35 μs, and approximately 12 traps are filled per pico-coulombs of charge for a 30-μm-diameter APD. Jensen *et al.* have published more detail on near-room-temperature GM-APD afterpulsing characterization [22]. Giudice *et al.* previously developed a similar technique for characterizing Si APDs [23].

By performing a double-gated afterpulse measurement on APDs with different absorber layers, the physical location of the dominant trap can be investigated. As shown in Fig. 22, APDs with different absorber layers operated at the same temperature show a similar initial, dominant detrapping time constant. Not only are the absorber layers different for these three APDs (InGaAs for the 1.55 μm APD, InGaAsP for the 1.06 μm APD, and InP for the all-InP dummy APD), but also the 1.06 and 1.55 μm APDs have graded transition layers between the field stop and the absorber while the all-InP dummy APD does not. Because the initial time constant is similar despite the differences in layer structure, our hypothesis is that the trap is located in one of the regions common to all three structures, namely, the field stop, multiplication, or p$^+$ anode region. The 250 K data indicate that more than one trap is important in determining the afterpulsing behavior at low temperature. The identification and characterization of these traps is an area of current research.

The trap responsible for afterpulsing in InP APDs (E_a $\sim$0.15 eV) may be the 0.42 eV trap level measured in DLTS, as described in Section V-A. If so, the difference between the apparent trap-energy levels would be due to the near-zero electric field in the device during the DLTS measurements. In contrast, the afterpulse measurements utilize an electric field near the breakdown field. The high electric field in the afterpulse measurements causes barrier lowering. Therefore, the trap will appear to have lower activation energy than its actual location within the bandgap. It is, however, possible that the afterpulsing trap level occurs at a concentration below the detection limit of the DLTS apparatus, and that the 0.42 eV DLTS level plays a role only as a DCR mechanism.

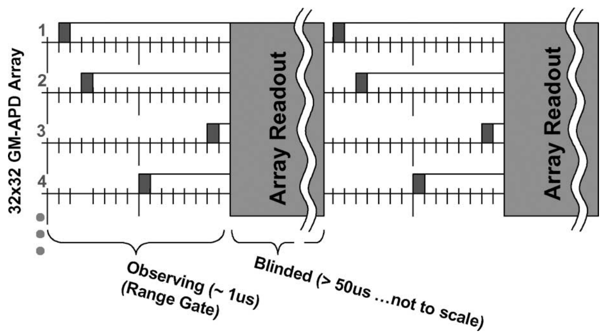

Fig. 23. Framed ROIC operating at low duty cycle. Photon time-of-arrival is captured during the range gate. Array readout occurs between flash LADAR returns.

VI. Readout Integrated Circuits

Section I introduced the various array formats for ROICs that have been developed for both deep-space LCs and for LADARs. This section describes the differences between framed ROICs and those with automatic pixel reset. Also described is the concept of a saturation flux of photons for GM-APD arrays and how it applies to both styles of ROIC.

A. Framed ROICs

Framed ROICs have been described by Aull *et al.* [4] and operate as shown in Fig. 23. A system controller sends an *arm* pulse (several nanoseconds long) to the focal plane that overbiases all of the APDs at once. The controller then sends a longer *range-gate* pulse (several microseconds) that operates CMOS timing circuits behind each of the pixels. Each time a photon is detected by an APD, the corresponding timing circuit stops counting and latches the time-of-arrival for that photon with $\sim$0.5 ns precision. At the end of the range-gate pulse, all of the time-stamp values as well as the detection locations are shifted off the ROIC into a field-programmable gate array (FPGA) by a readout clock. This procedure typically takes 20–50 μs, and the array is insensitive to any signal photons during readout.

The JIGSAW system is a compact flash LADAR system that uses a passively Q-switched microchip YAG laser as its transmitter [2]. These transmitters typically operate at pulse-repetition frequencies of 10–20 kHz. For the JIGSAW system, framed ROICs are the best choice for two reasons. First, the large signal gain of the GM-APD allow relatively few transistors ($<$100) to perform all the functions required by the pixel. We exploited this in recent designs by reducing the pixel pitch from 100 to 50 μm. Second, the pixel circuits only dissipate substantial electrical power during the range gate. Recent designs exploit this by scaling to larger formats (e.g., 128×32 and 256×64).

The ROIC pictured in Fig. 24 is the 32×32 ROIC, reported previously [4]. The current version offers improved time resolution ($<$0.5 ns), external clocking, and reduced power dissipation. InP-based detectors on this ROIC are currently operational at 1.06 and 1.55 μm wavelengths. Silicon APDs on this ROIC—such as were used in JIGSAW—operated at 0.53 μm wavelength.

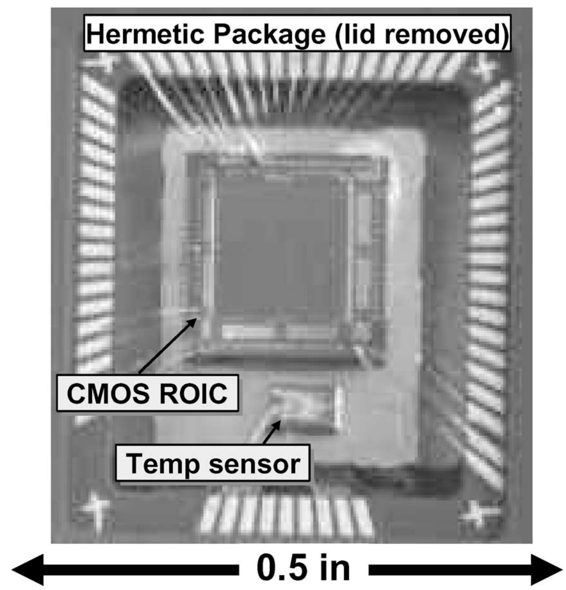

Fig. 24. Packaged 32×32 APD array on a framed ROIC. The CMOS ROIC, and InP APDs, GaP microlenses were stacked and copackaged with a temperature sensor onto an in-package thermoelectric cooler.

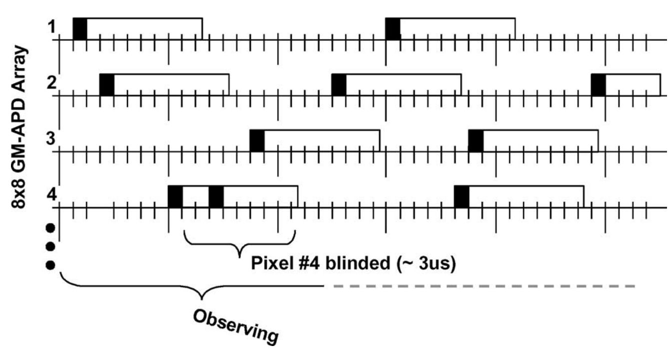

Fig. 25. Timing diagram depicting the automatic reset capability of an ROIC appropriate for detecting continuous signals, as in the LCs application.

B. ROICs With Automatic Pixel Reset

ROICs with automatic pixel reset can support a continuous mode of readout, in which signal photons impinge on the array continuously (or at high duty cycle) and the corresponding time stamps and location information continuously flow off chip. Such an ROIC is only limited in its availability to detect by the intrinsic reset time T_R of the APDs. Fig. 25 shows schematically how pixels behave in these ROICs.

Each line in Fig. 25 depicts the behavior of 1 of the 64 pixels on a time line. For example, pixel 1 detects a photon (black), outputs the time stamp when polled by RESET (not shown), and then, leaves the APD in the disarmed state (gray) until all carriers have escaped the multiplier to reduce afterpulsing. Then pixel 1 is rearmed until a dark count (black) starts the process again. In contrast to previously reported LADAR ROICs, the other pixels are unaffected by the behavior of pixel 1. Therefore, the

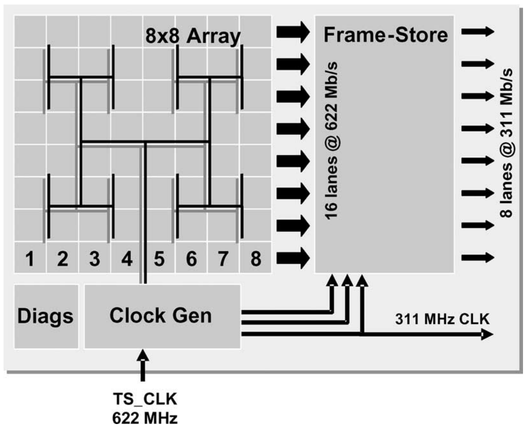

Fig. 26. Block diagram of the MLCD ROIC.

photon flux at which this array saturates is much higher than an equivalent array with a LADAR-style ROIC that typically operates near 2% duty cycle. However, the array can still saturate because of the finite reset time needed to avoid afterpulsing. Pixel 4 depicts this behavior when two signal photons impinge too closely in time. The first signal photon causes the APD to fire and the second signal photon is not detected since the APD is still disarmed.

The CMOS ROIC developed for the MLCD mission comprises four functional blocks that are shown in its floor plan in Fig. 26. An 8×8 array of pixel circuits has exposed nickel-plated pads for bump-bond connection to the InP APD array. The pixel circuits are on a $100\,\mu$m pitch and are responsible for arming and disarming the APD, detecting and time stamping a firing event, and for switching the time-stamp register in and out of the data output path to the frame store. The frame store receives time stamps from the pixel circuits and streams them off chip over eight 3.3 V low-voltage CMOS (LVCMOS) connections to an FPGA at a reduced rate. The clock generator distributes the master time-slot clock (TS_CLK, which has been operated up to 622 MHz) that determines the timing resolution of the ROIC. It also derives and distributes a STROBE clock (4.9 MHz) that periodically polls the 8×8 array and signals the pixel circuits to output any time-stamp data to the frame store. The diagnostics section was used to verify the ROIC design but is not normally used as part of the detector.

Fig. 27 shows a simplified schematic diagram of pixels 6, 7, and 8 in a single row of the 8×8 array depicted in Fig. 26. A linear-feedback shift register functions as the high-speed counter whose state is frozen when the APD fires. The APD is immediately disarmed by an active quench circuit, and the pixel waits until a STROBE clock rising edge to switch the shift register with its frozen time stamp into the output path to the frame store. After the time stamp is transferred out, the APD stays disarmed for eight ticks of the STROBE clock (about $1.6\,\mu$s with STROBE at 4.9 MHz) until it is finally rearmed and ready to detect photons.

The ROIC was fabricated using a $0.35\,\mu$m CMOS process at a commercial foundry. It uses 5 and 3.3 V supply voltages for biasing the APDs and driving logic circuits, respectively. The

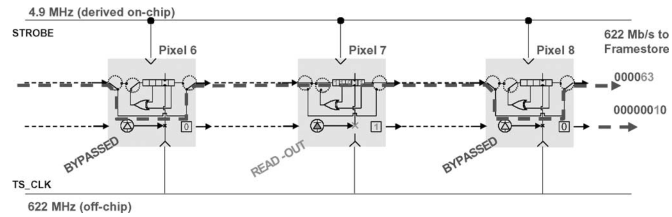

Fig. 27. Simplified schematic of pixel circuits for the 8×8 MLCD ROIC.

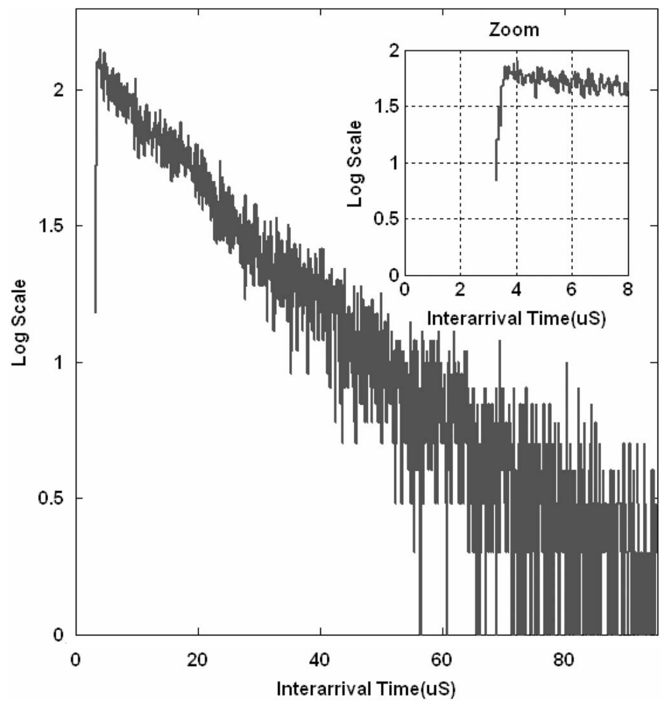

Fig. 28. Measured interarrival times for dark counts on a single pixel in the 8×8 array. A Poisson-like behavior is apparent for interarrival times longer than the $3.6\,\mu$s reset time.

ROIC was connected to an FPGA with standard LVCMOS–low voltage differential signal (LVDS) converter chips. The APD arming circuit supports up to 5 V of overbias and a variable avalanche detection threshold.

Fig. 28 shows a histogram of the time between APD firings (interarrival time) for a single detector. The pixel is not illuminated, so every firing is caused by primary dark current. The ROIC in this case was operated at room temperature with a 311-MHz clock resulting in a dead time of $3.2\,\mu$s. Consequently, there are no interarrival times less than that in the figure. The absence of any significant afterpulsing can also be inferred from the lack of a sharp peak at the onset of firing. Because the dark counts are a Poisson process, the interarrival times are exponentially distributed with the Poisson rate parameter, and thus, the data in Fig. 28 can be used to estimate a DCR of 40 kHz.

The inset in Fig. 28(b) is an expanded view and shows the $3.2\,\mu$s reset time. Due to the reset time, the behavior of a single APD is non-Poisson. Signal light can illuminate multiple APD pixels to form a macropixel that can mask the effect of the dead time so that it is statistically unlikely that two or more photons will impinge on the same pixel within one reset time. In this case,

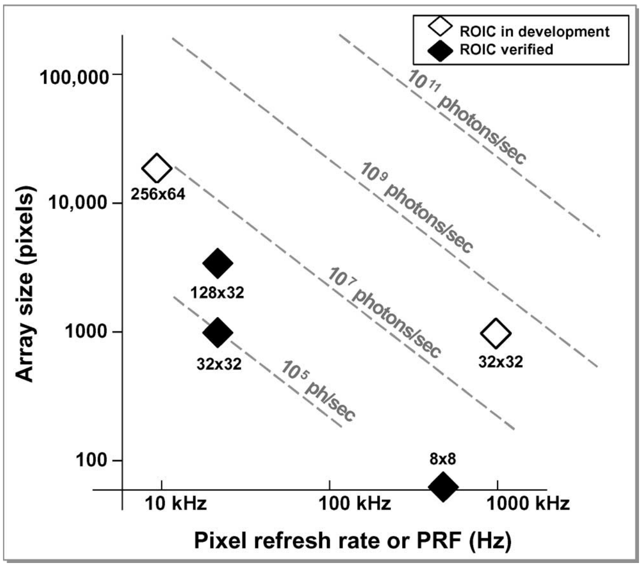

Fig. 29. CMOS ROICs plotted by array size versus pixel refresh rate or pulse-repetition frequency for a transmitter. Lines of constant saturation flux are overlaid.

the measured interarrival times can be arbitrarily small when two or more APDs in the same macropixel fire simultaneously. This results in nearly ideal Poisson behavior for a communications channel using macropixels. The Poisson channel behavior simplified the design of the forward-error correction codes for the MLCD mission [24].

C. Photon Flux for Array Saturation

A trade space for ROIC design is described in Fig. 29. Framed ROICs operate at modest duty cycle but can consume little power per pixel, and consequently, can be scaled to large array formats. These ROICs typically operate between 10 and 20 kHz pulse-repetition rate and can support as many as $16,384$ pixels. The rectangular format of these ROICs eases the input/output routing, and is easily tolerated by a beam-shaping optic in the rear of the telescope. ROICs with continuous readout have many more transistors per pixel and dissipate more electrical power. They can asynchronously reset APD pixels in times as short as $1\ \mu$s. A recent design that is currently under test has scaled the MLCD 8×8 array to a 32×32 format.

An important figure of merit for GM-APD arrays is their saturation flux. There are many ways to describe saturation. We use the flux *detected* by the array that reduces the likelihood of an additional photon being detected by $\sim$1 dB—in analogy to the zero-background blocking loss described in Section II-B. In this case, the saturation flux S is defined by $10\ \log_{10}[1 + (ST_r/N)] = 1$ dB, where N is the number of pixels in the array and T is the effective reset time or frame period for rearming an APD in a particular ROIC. In this definition, the detector array begins saturating when $ST_r/N \approx 0.25$, and a signal-induced blocking loss of $\sim$1 dB has to be accommodated in the system link budget.

VII. Summary

Arrays of GM-APDs coupled to CMOS ROICs demonstrated photon-counting behavior in a form factor that is well suited for 3-D imaging and LCs. Dynamic range can be increased by using concepts such as macropixels and continuous-mode reset. These concepts have been experimentally demonstrated and are equivalent to the use of oversampling to achieve dynamic range by 1-bit analog-to-digital converters. Compared to alternative receivers with photon-counting sensitivity, receivers using GM-APD arrays have unrivaled size, weight, power, and imaging capability.

Acknowledgment

The authors acknowledge Dr. M. Kesler of Widenet for writing the microlens encircled energy software and 4GEN Research, LLC, for performing DLTS measurements and analysis on our materials.

References

[1] K. A. McIntosh, J. P. Donnelly, D. C. Oakley, A. Napoleone, S. D. Calawa, L. J. Mahoney, K. M. Molvar, E. K. Duerr, S. H. Groves, and D. C. Shaver, "InGaAs/InP avalanche photodiodes for photon counting at 1.06 μm," *Appl. Phys. Lett.*, vol. 81, pp. 2505–2507, 2002.
[2] R. M. Marino and W. R. Davis, "JIGSAW: A foliage-penetrating 3D imaging laser radar system," *MIT Lincoln Lab. J.*, vol. 15, pp. 23–36, 2005.
[3] D. M. Boroson, A. Biswas, and B. L. Edwards, "MLCD: Overview of NASA's Mars Laser Communications Demonstration System," *Proc. SPIE*, vol. 5338, pp. 16–28, 2004.
[4] B. F. Aull, A. H. Loomis, D. J. Young, R. M. Heinrichs, B. J. Felton, P. J. Daniels, and D. J. Landers, "Geiger-mode avalanche photodiodes for three-dimensional imaging," *Lincoln Lab. J.*, vol. 13, pp. 335–350, 2002.
[5] C. Niclass, A. Rochas, P.-A. Besse, and E. Charbon, "Design and characterization of a CMOS 3-D image sensor based on single photon avalanche photodiodes," *IEEE J. Solid-State Circuits*, vol. 40, no. 2, pp. 1847–1854, Sep. 2005.
[6] S. Cova, M. Ghioni, A. Lotito, E. Rech, and F. Zappa, "Evolution and prospects for single-photon avalanche diodes and quenching circuits," *J. Mod. Opt.*, vol. 51, no. 2, pp. 1267–1288, 2004.
[7] R. Ben-Michael, M. A. Itzler, B. Nyman, and M. Entwistle, "Afterpulsing in InGaAs/InP single photon avalanche photodetectors," in *2006 Dig. LEOS Summer Top. Meetings*, Quebec City, QC, Canada, Jul. 17–19, 2006, IEEE Cat. No. 06TH8863C, pp. 15–16.
[8] J. P. Donnelly, E. K. Duerr, K. A. McIntosh, E. A. Dauler, D. C. Oakley, S. H. Groves, C. J. Vineis, L. J. Mahoney, K. M. Molvar, P. I. Hopman, K. E. Jensen, G. M. Smith, S. Verghese, and D. C. Shaver, "Design considerations for 1.06-μm InGaAsP-InP Geiger-mode avalanche photodiodes," *IEEE J. Quantum Electron.*, vol. 42, no. 8, pp. 797–809, Aug. 2006.
[9] G. B. Stringfellow, *Organometallic Vapor-Phase Epitaxy,* 2nd ed. Academic Press, San Diego, CA, 1999, ch. 8, pp. 421–427.
[10] W. A. Anderson and K. L. Jiao, *Indium Phosphide and Related Materials: Processing, Technology, and Devices*, A. Katz, Ed. Artech House, Bostan, MA, pp. 82–102.
[11] A. P. Seitsonen, R. Virkkunen, M. J. Puska, and R. M. Nieminen, "Indium and phosphorous vacancies and antisites in InP," *Phys. Rev. B*, vol. 49, pp. 5253–5262, 1994.
[12] K. Eguchi, Y. Ohba, M. Kushibe, M. Funamizu, and T. Nakanisi, "Effects of growth parameters on layer properties for InP and related alloys grown by MOCVD," *J. Cryst. Growth*, vol. 93, no. 8, pp. 88–92, 1988.
[13] S. Pellegrini, R. E. Warburton, L. J. J. Tan, J. S. Nv, A. B. Krysa, K. Groom, J. P. R. David, S. Cova, M. J. Robertson, and G. S. Buller, "Design and performance of an InGaAs-InP single-photon avalanche diode detector," *IEEE J. Quantum Electron.*, vol. 42, no. 4, pp. 397–403, Apr. 2006.
[14] M. A. Itzler, R. Ben-Michael, C.-F. Hsu, K. Slomkowski, A. Tosi, S. Cova, F. Zappa, and R. Ispasoiu, "Single photon avalanche diodes (SPADs) for 1.5 μm photon counting applications," *J. Mod. Opt.*, vol. 54, no. 4, pp. 283–304, 2007.

[15] G. Hasnain, W. G. Bi, S. Song, J. T. Anderson, N. Moll, C. Su, J. N. Hollenhorst, N. D. Baynes, I. Athroll, S. Amos, and R. M. Ash, "Buried-mesa avalanche photodiodes," *IEEE J. Quantum Electron.*, vol. 34, no. 12, pp. 2321–2326, Dec. 1998.

[16] I. Watanabe, M. Tsuji, M. Hayashi, K. Makita, and K. Taguchi, "Reliability of mesa-structure InAlGaAs–InAlAs superlattice avalanche photodiodes," *IEEE Photon. Technol. Lett.*, vol. 8, no. 6, pp. 824–826, Jun. 1996.

[17] S. Smetona, K. Klunder, S. An, R. Rousina-Webb, B. Emmerstorfer, E. Jamroz, M. Rouabhi, and R. Mallard, "Reliability of InP-based avalanche photodiodes for high bit-rate fiber-optic communication systems," in *Proc. InP Relat. Mater. Conf.*, 2002, pp. 373–376.

[18] G. M. Smith, J. P. Donnelly, K. A. McIntosh, E. K. Duerr, C. J. Vineis, D. C. Shaver, S. Verghese, J. E. Funk, J. M. Mahan, P. I. Hopman, L. J. Mahoney, K. M. Molvar, F. J. O'Donnell, D. C. Oakley, and K. G. Ray, "Design and reliability of mesa-etched InP-based Geiger-mode avalanche photodiodes," presented at the Conf. Lasers Electro-Opt. 2006 Tech. Dig., Long Beach, CA, Paper CThD7.

[19] Z. L. Liau, "Mass transport: Semiconductor microstructure fabrication by surface energy," *Mater. Sci. Eng. R: Rep.*, vol. R42, pp. 41–63, 2003.

[20] Zygo Corp., (2006). Middlefield, CT. Zygo new view 6000 series. White light interferometer.

[21] E. A. Dauler, P. I. Hopman, K. A. McIntosh, J. P. Donnelly, E. K. Duerr, R. J. Magliocco, L. J. Mahoney, K. M. Molvar, A. Napoleone, D. C. Oakley, and F. J. O'Donnell, "Scaling of dark count rate with active area in 1.06 μm photon-counting InGaAsP/InP avalanche photodiodes," *Appl. Phys. Lett.*, vol. 89, pp. 111102-1–111102-3, 2006.

[22] K. E. Jensen, P. I. Hopman, E. K. Duerr, E. A. Dauler, J. P. Donnelly, S. H. Groves, L. J. Mahoney, K. A. McIntosh, K. M. Molvar, A. Napoleone, D. C. Oakley, S. Verghese, C. J. Vineis, and R. D. Younger, "Afterpulsing in Geiger-mode avalanche photodiodes for 1.06 μm wavelength," *Appl. Phys. Lett.*, vol. 88, pp. 133503-1–133503-3, 2006.

[23] A. C. Giudice, M. Ghioni, S. Cova, and F. Zappa, "A process and deep level evaluation tool: Afterpulsing in an avalanche junction," in *Proc. Eur. Solid-State Device Res. Conf. (ESSDERC 2003)*, pp. 347–350.

[24] P. I. Hopman, P. W. Boettcher, L. M. Candell, J. B. Glettler, R. Shoup, and G. Zogbi, "An end-to-end demonstration of a receiver array based free-space photon counting communications link," *Proc. SPIE*, vol. 6304, pp. H1–H13, 2006.

Simon Verghese (S'85–M'87) received the B.S. degree in physics and a second B.S. degree and the M.S. degree in electrical engineering from the North Carolina State University, Raleigh, in 1987, and the M.A. and Ph.D. degrees in physics from the University of California, Berkeley, in 1993.

During 1993, he was a Postdoctoral Associate in the Department of Electrical Engineering and Computer Science, Massachusetts Institute of Technology (MIT), Cambridge. In 1995, he joined the Technical Staff, MIT Lincoln Laboratory, Lexington, where he was engaged in terahertz photomixers, resonant-tunneling diodes, infrared and UV avalanche photodiodes, and their associated readout integrated circuits. Then, he joined PhotonEx Corporation, a fiber-optic communications company. In 2003, he rejoined MIT Lincoln Laboratory, where he is currently an Assistant Leader of the Electro-Optical Materials and Devices Group.

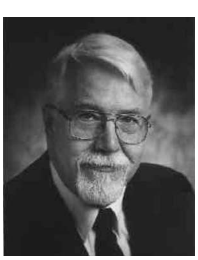

Joseph P. Donnelly (S'60–M'63–SM'88–F'90–LF'05) received the Bachelor's degree from Manhattan College, Bronx, NY, in 1961, and the M.S. and Ph.D. degrees from Carnegie Mellon University, Pittsburgh, PA, in 1962 and 1966, respectively, all in electrical engineering.

He was a North Atlantic Treaty Organisation (NATO) Postdoctoral Fellow at Imperial College, London, U.K. He is currently a Senior Staff Member at Lincoln Laboratory, Massachusetts Institute of Technology, Lexington. He is also an Adjunct Professor in the Physics Department, University of Massachusetts Lowell, Lowell. His current research interests include high-power semiconductor lasers, integrated optics, and avalanche photodiodes.

Dr. Donnelly is a member of the Bohmesche Physical Society, Eta Kappa Nu, and Sigma Xi. He was a National Lecturer for the IEEE Electron Devices Society in 1979. In 2001, he was a Guest Associate Editor for a special issue of the IEEE JOURNAL OF SELECTED TOPICS IN QUANTUM ELECTRONICS on semiconductor lasers, and from 2002 to 2004, he was an Associate Editor of the IEEE JOURNAL OF QUANTUM ELECTRONICS.

Erik K. Duerr received the B.S. degree from the University of Virginia, Charlottesville, in 1995, and the S.M. and Ph.D. degrees from Massachusetts Institute of Technology (MIT), Cambridge, MA in 1998 and 2002, respectively, all in electrical engineering.

In 2003, he joined MIT Lincoln Laboratory, Lexington, where he is currently developing avalanche photodiodes for single-photon detection using a variety of III–V material systems.

K. Alex McIntosh received the B.S. degree in physics from the University of California, Davis, in 1986.

He is a member of the Electro-Optical Materials and Devices Group, Lincoln Laboratory, Massachusetts Institute of Technology, Lexington, where he has investigated high-speed infrared detectors, terahertz photomixers, and photonic crystal structures for infrared and microwave applications. His current research interests include the development of arrays of Geiger-mode avalanche photodiodes.

David C. Chapman received the B.S. and Ph.D. degrees from the Materials Science and Engineering Department, University of Utah, Salt Lake City, in 1999 and 2004, respectively.

Since 2005, he has been a Member of the Technical Staff, Lincoln Laboratory, Massachusetts Institute of Technology (MIT), Lexington, where he is engaged in the OMVPE growth and characterization of thermophotovoltaics and Geiger-mode avalanche photodiodes. His current research interests include OMVPE growth and characterization of III–V materials with a focus on understanding how growth conditions influence materials properties and how that relates to device performance.

Christopher J. Vineis received the B.S.E. degree from the University of Pennsylvania, Philadelphia, in 1996, and the Ph.D. degree from Massachusetts Institute of Technology (MIT), Cambridge, in 2001, both in materials science and engineering .

Since 2005, he has been a Member of the Technical Staff, MIT Lincoln Laboratory, Lexington, where he is engaged in high-figure-of-merit nanostructured thermoelectric films for power generation and cooling applications, as well as Geiger-mode avalanche photodiodes for single-photon detection. His current research interests include materials growth and characterization and the relationship between device performance and materials properties, with a particular focus on electronic and optoelectronic materials and devices. He has experience with a variety of Si, III–V, and IV–VI materials systems, as well as lattice-mismatched epitaxy and metrology.

Gary M. Smith (S'93–M'95–SM'06) received the B.S., M.S., and Ph.D. degrees from the University of Illinois, Urbana-Champaign, in 1991, 1992, and 1996, respectively, all in electrical engineering.

In 1995, he joined Advanced Technology Materials, Inc., Dallas, TX, where he researched optoelectronic devices in wide bandgap semiconductors. In 1999, he joined Corning Lasertron, Dallas, TX, where he was involved in the development of high-power 980-nm pump lasers, and led the new product introduction of 250 and 500 mW fiber grating stabilized pump lasers. In 2004, he joined Lincoln Laboratory, Massachusetts Institute of Technology (MIT), Lexington, where he developing optoelectronic semiconductor devices, and is primarily focusing on Geiger-mode avalanche photodiode arrays.

Josephy E. Funk is a member of the Electro-Optical Materials and Devices Group, Lincoln Laboratory, Massachusetts Institute of Technology, Lexington, where he has developed several automated test systems used in the measurement and characterization of avalanche photodiode arrays. His current research interests include the research and development of Geiger-mode avalanche photodiode arrays and active alignment and attachment of microlens arrays.

Katharine Estelle Jensen was born in New Haven, CT, in 1982. She received the A.B. degree in physics from Princeton University, Princeton, NJ, in 2004.

Since 2004, she has been a member of the Electro-Optical Materials and Devices Group, Lincoln Laboratory, Massachusetts Institute of Technology, Lexington. She is also in the Department of Physics, Harvard University, Cambridge, MA.

Ms. Jensen is a member of Sigma Xi.

Pablo I. Hopman received the B.S. degree in physics from the University of California at Davis, Davis, in 1993, and the Ph.D. degree in physics from Cornell University, Ithaca, NY, in 2000.

In 2000, he joined Lincoln Laboratory, Massachusetts Institute of Technology, Lexington, where he is currently a Senior Staff Member in the Advanced Concepts and Technology Group. He has worked on the Mars Laser Communications Program where he served as a Lead Engineer for the detector subsystem and as a System Engineer for the ground receiver array. He has contributed to system studies, hardware development, and experimentation in several electrooptics areas, including photon counting communications, and space surveillance.

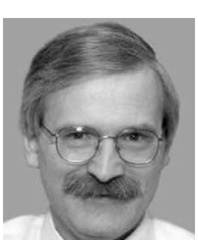

David C. Shaver (M'91–SM'04) received the S.B., S.M., and Ph.D. degrees in electrical engineering from Massachusetts Institute of Technology (MIT), Cambridge, in 1976, 1978, and 1981, respectively.

In 1977, he joined the MIT Lincoln Laboratory, Lexington, in the area of submicrometer structure fabrication, where he applied X-ray and e-beam lithography to the fabrication of both electronic devices, such as submicrometer channel-length silicon MOSFETs and diffractive optics, including Fresnel zone-plates used for X-ray imaging. He has developed electron-beam techniques for testing and repairing wafer-scale integrated circuits. In 1984, he joined a start-up company, Micrion Corporation, where he was the Chief Scientist and the Director of Research, and was engaged in developing focused ion-beam and laser-beam microchemistry systems for photomask, microcircuit, and flat-panel display repair and modification.

In 1988, he rejoined MIT Lincoln Laboratory, where he led a group that pioneered the development of 193-nm-wavelength optical lithography, and in the fall of 1991, he became the Director of the Microelectronics Laboratory and the Assistant Head of the Solid State Division, and since 1994, he has been the Head of the Solid State Division. His current research interests include high-performance imaging sensors, deeply scaled silicon microelectronics, solid state lasers, optoelectronics, photonics, superconductive devices, quantum computing, biological agent sensors, microelectronics, circuit design, and neuroscience.

Brian F. Aull (S'76–M'84–SM'00) received the B.S. degree from Purdue University, West Lafayette, IN, in 1977, and the M.S. and Ph.D. degrees from Massachusetts Institute of Technology (MIT), Cambridge, in 1979 and 1985, respectively, all in electrical engineering.

He was a Member of the Technical Staff, Naval Avionics Center, Indianapolis, IN, in 1977 and 1979, and at Hewlett-Packard Laboratories, Palo Alto, during 1979–1980. During 1990–1991, he was a Visiting Professor in the Electrical Engineering Department, National Cheng-Kung University, Tainan, Taiwan. He is currently a Member of the Technical Staff, Advanced Imaging Technology Group, MIT Lincoln Laboratory, Lexington. His current research interests include solid-state materials and device technology for optoelectronic applications, and particularly for advanced imaging capabilities. He has developed focal plane arrays based on the integration of Geiger-mode avalanche photodiodes with digital CMOS timing and counting circuits.

Joseph C. Aversa photograph and biography not available at the time of publication.

Jonathan P. Frechette received the B.S. degree in electrical engineering in 2005 from the Northeastern University, Boston, MA, where he is currently working toward the M.S. degree.

He joined the Lincoln Laboratory, Massachusetts Institute of Technology, Lexington, in 2001 as a Co-Op Student, and in 2005, became an Assistant Staff Member in the Electro-Optical Materials and Devices Group, where he is currently engaged in the design and testing of readout integrated circuits.

James B. Glettler received the B.S. degree in electrical engineering from the University of Michigan, Ann Arbor, in 2003. He will be entering graduate studies in electrical engineering at Massachusetts Institute of Technology (MIT), Cambridge, in September 2007.

In 2004, he joined the MIT Lincoln Laboratory, Lexington, where he is currently an Associate Staff Member in the Advanced Space Systems and Concepts Group and is the Lead Receiver Engineer for a photon counting communication system following work on the Mars Laser Communication Program. He is also a Lead Hardware Engineer for a very-high-pixel-count video camera system.

Zong Long Liau received the B.S. degree in physics from the National Taiwan University, Taipei, Taiwan, in 1972, and the Ph.D. degree in applied physics from the California Institute of Technology, Pasadena, in 1979.

Since December 1978, he has been a Staff Member in the Electro-Optical Materials and Devices Group, Lincoln Laboratory, Massachusetts Institute of Technology, Lexington. He has pioneered a mass transport process for semiconductor microstructures, with which he demonstrated a first surface-emitting diode laser array, and a wafer fusion process (also known as direct wafer bonding or diffusion bonding), which has stimulated a wide range of new device applications. Since 2000, he has been engaged in highly powerful microoptics, and has contributed to several laser- and detector-array applications.

Dr. Liau was an Associate Editor for the IEEE JOURNAL OF QUANTUM ELECTRONICS from 1993 to 2002.

Joseph M. Mahan is an Assistant Staff Member of the Electro-Optical Materials and Devices Group, Lincoln Laboratory, Massachusetts Institute of Technology, Lexington. He has worked in the areas of metrology, tactical IR weaponry, process analytical spectroscopy, process control systems, and software test automation. His current research interests include test automation in support of avalanche photodiode development.

Leonard J. Mahoney (S'88–M'89) received the B.S. degree (with honors) in mechanical engineering from the Northeastern University, Boston, MA, in 1975.

In 1972, he joined Lincoln Laboratory, Massachusetts Institute of Technology, Lexington, where he has worked on process development and fabrication of microwave and electrooptic devices, and is currently an Associate Staff Member in the Electro-Optical Materials and Device Group, working on several InP- and GaN-based devices.

Karen M. Molvar received the B.S. degree in textile science from the University of Wisconsin, Madison, in 1978.

In 1980, she joined Lincoln Laboratory, Massachusetts Institute of Technology, Lexington, where she worked on a number of microwave devices and circuits including surface-oriented mixer diodes, frequency doublers, and FETs, and is currently a Project Technician in the Electro-Optical Materials and Device Group, working on GaN and InP devices.

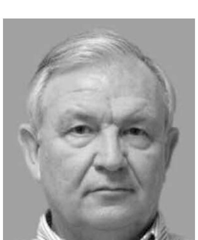

Frederick J. O'Donnell received the A.S. degree in electrical engineering from the Northeastern University, Boston, MA, in 1977.

In 1973, he joined Lincoln Laboratory, Massachusetts Institute of Technology, Lexington, where he is currently an Assistant Staff Member in the Electro-Optical Materials and Device Group and has worked on optical device testing, process development, and device fabrication for a variety of III–V materials, most recently on the Geiger-mode avalanche photodiodes.

Douglas C. Oakley received the B.A. degree from the University of Maine, Orono, 1991, and the M.S. degree from the University of Massachusetts, Lowell, in 1996, both in physics.

In the fall of 1996, he joined the Electro-Optical Materials and Devices Group, Lincoln Laboratory, Massachusetts Institute of Technology, Lexington, as an Assistant Research Staff, where he is currently an Associate Staff Member. He was engaged in the growth of novel GaSb-based materials by OMVPE for the thermophotovoltaics research effort, and in February 2001, got involved in the InP-based OMCVD materials growth effort, producing novel InP/InGaAs/InGaAsP-based avalanche photodiodes, p-i-n, laser, and modulator structures.

Edward J. Ouellette received the B.S. and S.M. degrees in 1994 from Massachusetts Institute of Technology (MIT), Cambridge, where he is currently working toward the Ph.D. degree, all in electrical engineering.

In 2005, he joined the Electro-Optical Materials and Devices Group, MIT Lincoln Laboratory, Lexington, where he is engaged in the development of CMOS photon-counting readout integrated circuits (ROICs), laser driver ICs, systems for communications, and 3-D LADAR applications. He has also been a Co-Op and a Consultant at Intel and Lucent, where he was engaged in extensive IC design and systems design.

Matthew J. Renzi received the B.S. degree in physics from the University of Massachusetts, Amherst, and the Ph.D. degree in applied physics from Cornell University, Ithaca, NY.

In 2003, he joined Lincoln Laboratory, Massachusetts Institute of Technology, Lexington, where he is currently a Staff Member in the Electro-Optical Materials and Device Group. He has worked on developing high-fill-factor Geiger-mode avalanche silicon photodiode arrays for photon counting applications.

Brian M. Tyrrell (S'97–M'98) received the S.M. degree from Massachusetts Institute of Technology (MIT), Cambridge, in 2004, and the B.S.E. degree from the University of Pennsylvania, Philadelphia, in 1998, both in electrical engineering.

He is currently a member of the Advanced Silicon Technology Group, MIT Lincoln Laboratory, Lexington, where he has been engaged in developing digitally dominated focal plane readout circuits spanning a wide range of wavelengths and applications and demonstration and characterization vehicles for MIT Lincoln Laboratory's advanced silicon processes, with a more recent focus on operation in extreme environments.